Subtle Changes in Hydrogen Bond Orientation Result in Glassification of Carbon Capture Solvents

Journal:	*Physical Chemistry Chemical Physics*
Manuscript ID	CP-ART-06-2020-003503.R1
Article Type:	Paper
Date Submitted by the Author:	07-Aug-2020
Complete List of Authors:	Banuelos, Jose; University of Texas El Paso Saunders, Steven; Washington State University Han, Kee Sung; Pacific Northwest National Laboratory Heldebrant, David; Pacific Northwest National Laboratory Dalgliesh, Robert; Science And Technologies Facility Council ISIS Neutron and Muon Source Headen, Thomas; Science And Technologies Facility Council ISIS Neutron and Muon Source Rousseau, Roger; Pacific Northwest National Laboratory Glezakou, Vanda; Pacific Northwest National Laboratory Graham, Trenton; Washington State University Malhotra, Deepika; Pacific Northwest National Laboratory Zhang, Difan; Pacific Northwest National Laboratory Nguyen, Manh-Thuong; Pacific Northwest National Laboratory Lee, Mal-Soon; Pacific Northwest National Laboratory Cantu, David; Pacific Northwest National Laboratory

SCHOLARONE™
Manuscripts

ARTICLE

Subtle Changes in Hydrogen Bond Orientation Result in Glassification of Carbon Capture Solvents

José Leobardo Bañuelos,[c] Mal-Soon Lee,[a] Manh-Thuong Ngyuen,[a] Difan Zhang,[a] Deepika Malhotra,[b] David C. Cantu,[a] Vassiliki-Alexandra Glezakou,[a] Roger Rousseau,[a] Thomas F. Headen,[d] Robert M. Dalgliesh,[d] David J. Heldebrant,[b,e]* Trent R. Graham,[a,e] Kee Sung Han[a] and Steven R. Saunders.[e]

Water-lean CO_2 capture solvents show promise for more efficient and cost-effective CO_2 capture, although their long-term behavior in operation has yet to be well studied. New observations of extended structure solvent behavior show that some solvent formulations transform into a glass-like phase upon aging at operating temperatures after contact with CO_2. The glassification of a solvent would be detrimental to a carbon-capture process due to plugging of infrastructure, introducing a critical need to decipher the underlying principles of this phenomenon to prevent it from happening. We present the first integrated theoretical and experimental study to characterize the nano-structure of metastable and glassy states of an archetypal single-component alkanolguanidine carbon-capture solvent. and assess how minute changes in atomic-level interactions convert the solvent between metastable and glass-like states. Small-angle neutron scattering and neutron diffraction coupled with small- and wide-angle X-ray scattering analysis demonstrate that minute structural changes in solution precipitae reversible aggregation of zwitterionic alkylcarbonate clusters in solution. Our findings indicate that our test system, an alkanolguanidine, exhibits a first-order phase transition, similar to a glass transition, at approximately 40°C— close to the operating absorption temperature for post-combustion CO_2 capture processes. We anticipate that these phenomena are not specific to this system, but are present in other classes of colvents as well.. We discuss how in molecular-level interactions can have vast implications for solvent-based carbon-capture technologies, concluding that fortunately in this case, glassification of water-lean solvents can be avoided as long as the solvent is run above its glass transition temperature.

Introduction

The Earth has warmed by approximately 1.0°C since the industrial revolution due to anthropogenic CO_2 emissions. As global emissions continue to rise, warming is expected to reach 2°C by the end of this century. The recent report from the Intergovernmental Panel on Climate Change (IPCC) identifies carbon capture and sequestration as critical to keeping the Earth "well below" a 1.5°C above pre-industrial level warming scenario to minimize the effects of a warming climate on human life.[1] Ultimately, negative emission technologies will be needed to remove the CO_2 already in the atmosphere, but before those technologies come online, post-combustion carbon capture is needed to stop future anthropogenic emissions from increasing even further and exhausting Earth's

carbon budget.[2] Post-combustion capture technologies include solvents, membranes, and porous materials.[3] Regardless of technology, the ultimate driver that has limited widespread adoption of post-combustion carbon capture and storage (CCS) is cost. CCS is still far from affordable; commercial technologies cost at least $58/tonne CO_2.[4] The U.S. Department of Energy has set an ambitious cost target of $40/tonne CO_2 for post-combustion technologies by the year 2030. Solvent-based technologies are the most mature post-combustion CCS technology and are expected to be the quickest to market as they are undergoing testing at large-scale demonstrations.[5][6][7][8][9][10]

The main energetic driver for solvent-based technologies is the energy-intensive thermal regeneration of chemically-selective solvents. This energy can be reduced by lowering the water content of the solvent as it minimizes energy lost due to boiling and condensing of water. The past decade has seen a shift in solvent formulation toward "water-lean" solvents that comprise similar formulations to first- and second-generation aqueous amines, albeit with as little water as possible. All formulations of water-lean solvents are either (1) organic bases that chemically react with CO_2 to form either carbamate or alkylcarbonate ionic liquids or (2) solid/liquid carbamate or

alkylcarbonate salts dissolved in co-solvents.(11, 12) The low-water content in these solvents enables lower reboiler duties than first- and second-generation aqueous amines, making them potentially more efficient,(11, 13) though some recent lost-work analyses have questioned the performance benefits of water-lean solvents using first-generation CCS infrastructure when compared against second-generation amines using 21st century configurations.(14)

In the absence of water as a co-solvent, water-lean solvents have been shown to exhibit unique physical and thermodynamic properties that may be exploitable for efficiency or cost gains.(11) Properties exploited for efficiency gains include: polarity-swing-assisted regeneration to reduce reboiler temperatures by as much as 72°C; higher CO_2 solubility to drive faster absorption kinetics; and phase changes to concentrate the CO_2-rich solvent so less exogenous material is heated during regeneration.(15, 16) Not surprisingly, not all physical and thermodynamic properties of these solvents are beneficial to performance; thus, understanding the molecular-level behavior of these solvents is critical to maximizing their full potential while minimizing any limiting behaviors.

Our group has spent the past few years studying how and why these properties arise in concentrated solvents such as CO_2-binding organic liquids (CO$_2$BOLs). These solvents are single-component systems comprised of alkanolguanidine chemical moieties. Our recent studies have linked the kinetic and thermodynamic properties of CO$_2$BOLs to a heterogeneous (disparate ionic/non-ionic domain) structure that begins forming upon CO_2 fixation.(17, 18) 1-((1,3-dimethylimidazolidin-2-ylidene)amino)propan-2-ol (1-IPADM-2-BOL) is an archetypal alkanolguanidine derivative that we have studied extensively, noting that the molecular-level structure(17) is markedly different than that of non-ionic liquids (e.g., alcohols) and ionic liquids (e.g., [bmim][BF$_4$]).(19, 20) Recently, the heterogeneous solvent structure was experimentally confirmed using two- and three-dimensional speciation mapping of 1-IPADM-2-BOL measured from *in situ* liquid state secondary ion mass spectrometry (SIMS) data.(19) Molecular dynamic (MD) simulations have shown that the formation of strong hydrogen bond networks and clusters of zwitterionic carbonate greatly impact viscosity of the CO_2-rich solvents, limiting their performance with respect to heat exchange and pumping.(16, 21, 22) Alternately, the judicious placement of these hydrogen bonds, through careful solvent design, may also reduce the viscosity, by containing the hydrogen bonding within the molecule,(22) or by favoring a high population of neutral species.(23) We recently showed that such a heterogeneous structure could be responsible for the anomalously high CO_2 transport in many water-lean solvents,(24),(25) as the disparate regions of ionic clusters and aggregates provides pockets or channels within the fluid where CO_2 can readily diffuse and react with CO_2-free solvent.(17) Ultimately, the nanoscale heterogeneity of the solvent structure is a double-edged sword and needs to be fully characterized so that it can be controlled.

In this work, we employ new spectroscopic measurements and computations at length scales above *and* below previous studies to thoroughly measure the changes in the mesoscopic (> nm, < µm) molecular structure of alkanol guanidines as a function of CO_2 loading and temperature. We present a combined experimental (neutron, X-ray) and theoretical study of 1-IPADM-2-BOL as an archetypal water-lean solvent and assess how changes in the mesoscopic structure occur. We also present evidence for a previously undiscovered glass transition within 1-IPADM-2-BOL (and two other alkanolguanidine derivatives), indicating that this behavior may be common to other water-lean formulations. We close with a discussion of how minute changes in hydrogen bond partners within the fluid can influence the viability of these solvents for CO_2 capture in addition to ways to mitigate the potential for catastrophic plugging of a CCS unit during operation.

Results and discussion

Viscosity anomalies

Our first molecular simulations(22, 26) predicted the transition of free-flowing 1-IPADM-2-BOL and other alkanolguanidine liquids into what is best described as a "glassy state." Initial simulations were performed at a representative "CO_2-lean" of 0.25 mol CO_2/mol solvent and a "CO_2-rich" solvent loading of 0.50 mol CO_2/mol solvent to span the solvent's expected working range in a working process. Initial simulations of these two loadings showed higher viscosity values than experimental measurements of 1-IPADM-2-BOL. At the time, there had been no prior evidence (visual or measured) of glassification of 1-IPADM-2-BOL at ~40°C during continuous flow CO_2-absorption/desorption testing in our lab.(27) Our original observations of the glass-like appearance of 1-IPADM-2-BOL at room temperature, was attributed to the temperature dependence of viscosity of CO$_2$BOLs and other water-lean solvents.(28-32) Thus, it was not clear why simulations were predicting glassification at 40°C when it had not been measured experimentally.

To ascertain the nature of this dual state of the solvents, we synthesized a fresh batch of 1-IPADM-2-BOL and subjected it to measurements using a custom pressure-volume temperature (PVT) cell described previously.(18) The cell that was specifically designed to enable simultaneous vapor-liquid equilibria (VLE) was used for viscosity and kinetics measurements as a function of CO_2 loading. 1-IPADM-2-BOL was tested at 40°C (the estimated absorption temperature in a working process(33)), with one hour between CO_2 injections to allow the solvent to reach equilibrium. Interestingly, the viscosity of 1-IPADM-2-BOL (Figure 1, yellow circles, and Table SI1) was greater than our previously reported viscosity profile(34) and data for the solvent in continuous-flow operation. The higher viscosity profile was peculiar, as the viscosities for all three measurements were performed on the same viscometer at the same temperature on the same solvent. The difference in viscosity profiles was initially thought to be due to different CO_2 loadings, though the accompanying vapor liquid equilibrium

curves that were measured in both systems were well within experimental error.

The mismatch between the VLE and viscosity data led us to wonder whether or not the time between injections and measurement was the culprit. The previous viscosity profiles for 1-IPADM-2-BOL(34) were measured with a ~10-minute equilibration time between CO_2 injections, and in our continuous flow testing,(27) the residence time for the solvent leaving the absorber before regeneration in the stripper column was ~12 minutes. A second viscosity profile for 1-IPADM-2-BOL was measured under isothermal conditions (40°C) in our PVT cell, performing manual injections at forced 10-minute injection intervals, ensuring that the VLE and loading profile matched those for the measurement with an hour CO_2 injection interval.
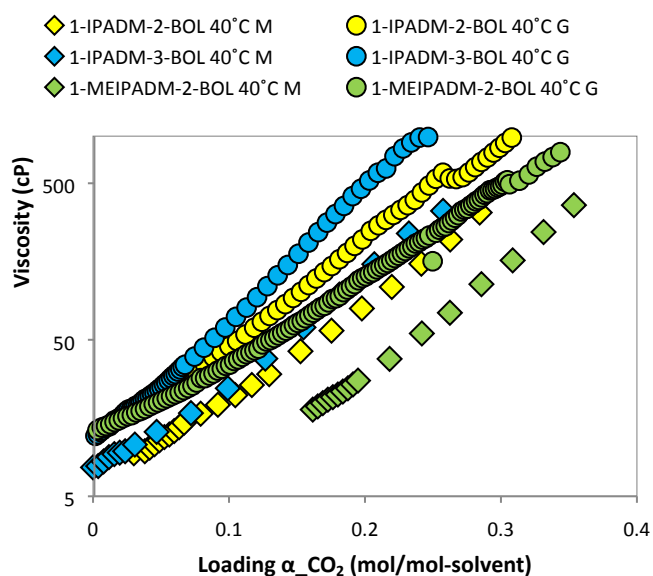

Figure 1. Viscosity profile for the metastable and glassy state for three alkanolguanidines as a function of CO_2 loading. Each derivative is represented in the same color as either circles (G = glassy) or diamonds (M = metastable).

Because one anomaly may not indicate a broader trend, we investigated whether disparate viscosity profiles were present in other alkanolguanidine formulations. Of the dozens of alkanolguanidine derivatives we have synthesized previously(18), we chose two other well-characterized derivatives (1-IPADM-3-BOL and 1-((1,3-dimethylimidazolidin-2-ylidene)amino)-3-methoxypropan-2-ol {1-MEIPADM-2-BOL}) and subjected them to the same viscosity and VLE measurements at 40°C as a function of CO_2 loading with 10-minute and 60-minute equilibration times between injections. 1-((1,3-dimethyltetrahydropyrimidin-2(1*H*)-ylidene)amino)propan-2-ol {1-IPADM-3-BOL} and 1-MEIPADM-2-BOL also showed different viscosity profiles at the exact same partial pressure of CO_2 (P*) (Figure 1, and Table SI1) indicating this phenomenon may be more common to alkanolguanidines than previously known.

In earlier wok, we reported that the viscosity increase in alkanolguanidine solvents is linked to the orientation of hydrogen bonding in solution, but we had never seen samples transition to a glassy state during measurements. (18, 26) The discovery of a second, more viscous, viscosity profile with no associated change in P* suggests that there must be a transformation in the molecular-level ordering within the fluid. We had previously observed >500 nm aggregates of zwitterionic guanidinium carbonates for 1-IPADM-2-BOL using two- and three-dimensional time-of-flight (ToF)-SIMS measurements, albeit at room temperature.(17) It was not clear whether such clustering contributed to the original or glassy-state viscosity profile. Further, it was unclear how and why these large aggregates form in solution, and perhaps even less clear why the glassification was being observed. As indicated above, initial simulations had not yet observed changes in longer range order, which may be attributed to the simulation boxe size (~8×8×8 nm). Thus, little was known about how the structural features within the solvent at length scales greater than our box size could be impacting the physical and thermodynamic properties of the solvent. Scattering methods that could identify such changes in the mesoscopic structure were needed to decipher how structural changes within the fluid were occurring and assess which structural features were converting these three alkanolguanidines into a newly discovered "glassy state."

Neutron Diffraction and Scattering of 1-IPADM-2-BOL

Neutron diffraction (ND) and small-angle neutron scattering (SANS) were employed to investigate the short-range molecular-scale interactions and nanoscale structural changes within the fluid to shed light on the structural details of 1-IPADM-2-BOL. SANS has been successfully used to characterize liquid-liquid structural heterogeneity (mass-fractal dimension (and aggregation behavior in water-alcohol mixtures.(35-37)

Measurements to observe the solvent's proposed mesoscopic heterogeneity require sufficient scattering contrast between the ionic and non-ionic domains within 1-IPADM-2-BOL when CO_2 is present. 1-IPADM-2-BOL was synthesized in various levels of deuteration to enhance the contrast between the CO_2-reacted and unreacted phases. Our efforts to synthesize fully deuterated target were not successful due to challenges with ring closure in the penultimate synthetic step, leaving us with a perdeuterated analogue, dimethyl (ethane-1,2-diyl-d4)bis((methyl-d3)carbamate). We note that alkanolguanidines always have at least 50% non-ionic co-solvent. This is in part due to alkanolguanidines reaching CO_2 saturation at 0.5 mol CO_2/mol solvent, leaving half of the solvent unreacted. Details of the synthetic methodology for the derivatives of 1-IPADM-2-BOL can be found in the experimental section below. In this work we hereafter refer to the tri-nitrogen guanidine core as the "head" and the alcohol chain as the "tail."
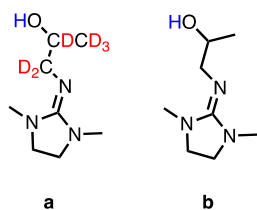
Figure 2. 1-IPADM-2-BOL with varied levels of deuteration used in this study: (a) per-proteo, (b) ½ proteo, ½ deuteron.

ND measurements were performed on the Near and InterMediate Range Order Diffractometer (NIMROD)(38) and SANS measurements on the "Larmor" (see SI) instrument, both at Target Station 2 of the ISIS neutron spallation and muon source in Oxfordshire, UK Experiments were performed at CO_2 loadings ranging in mole fractions from 0 to 0.5 and at temperatures ranging from 20–100°C, covering the expected loading and temperature operating ranges of a working process.
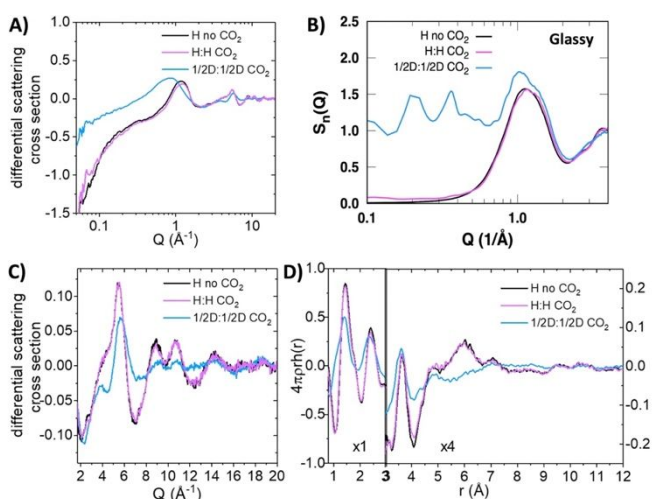

Figure 3. Experimental and simulated ND of H and ½D 1-IPADM-2-BOL mixtures with and without CO_2. The data in this figure were all collected at 40°C. Unless otherwise noted, the second component in the 1:1 molar mixture is fully loaded with CO_2. (A): Differential scattering cross-section (DCS) plots over the entire measured Q-range (log scale). (B) Simulated neutron diffraction at different deuteration levels showing qualitative agreement with the experimental data. (C) DCS plots zoomed in over Q = 2–20 Å^{-1}. (D) Plot of $4\pi\rho r h(r)$ vs. r correlation, where $h(r)$ is the Fourier transform of the DCS; the plot is magnified ×4 from 3 to 12 Å.

Each derivative of 1-IPADM-2-BOL (Figure 2) was handled under an inert atmosphere. The samples (as shown in Figure 2) were synthesized (CO_2-free) and fully saturated with CO_2 to represent extremes in CO_2 loading for the solvent. Individual and mixed samples were loaded into a cleaned and dry cell. The samples were inserted into the TiZr null scattering alloy holder in NIMROD and ND measurements were performed at constant temperature using a circulating oil bath connected to the cell. Measurements were performed to observe any changes in the solvent's structure as temperature was increased or decreased.

Diffraction data from the fully protonated sample (H) is very similar with and without CO_2 loading with the first diffraction peak at Q ≈ 1.18 Å^{-1}. The low-Q intensity increase in sample ½D:½D exhibits a large increase at low Q, a sharp diffraction peak near 0.85 Å^{-1}, and a broad g(r) peak at 7-9 Å, indicative of structural heterogeneity. The majority of atom-atom correlations < 4 Å in ND measurements were performed on the Near and InterMediate Range Order Diffractometer (NIMROD)(38) and SANS measurements on the "Larmor" (see SI) instrument, both at Target Station 2 of the ISIS neutron spallation and muon source in Oxfordshire, UK Experiments were performed at CO_2 loadings ranging in mole fractions from 0 to 0.5 and at temperatures ranging from 20–100°C, covering the expected loading and temperature operating ranges of a working process.

Figure 3(D) are intramolecular in nature and have the expected values for the chemical groups comprising the system. Temperature-dependent measurements over the solvent's expected temperature range in operation (40–100°C) yielded a slight increase in the differential scattering cross section (DCS) with temperature at Q-values below the first sharp diffraction peak, as expected for liquids because the DCS at Q = 0 is proportional to the isothermal compressibility (see Figure S1 in the SI). Mixtures with D showed the most variation with temperature, though the exact shape of the DCS for Q < 0.2 Å^{-1} may be impacted by some errors in the subtraction of the incoherent scattering contribution to the DCS which is particularly high for the light hydrogen isotope.

ND measurements of mixtures of the CO_2-bound protiated, partially deuterated (tail), and fully deuterated 1-IPADM-2-BOL liquid each highlight specific correlations that play a role in forming the disparate nano-environment within the fluid. For the first time, we characterized the interface morphology at the nanometer scale as a function of temperature and CO_2 loading.

We then compared the experimental data to simulation. Simulated ND data (Figure 3B) was obtained by analyzing the structures from classical molecular dynamic simulations.(39, 40) Consistent with experiment, all systems exhibit a strong peak is identified at ~1 Å^{-1} for the ½D:½D and ~1.1 Å^{-1} for no CO_2 and full CO_2 loading structures. The simulated ND results successfully captured the peak shift as well as the peak width of 1-IPADM-2-BOL with different levels of deuteration at ~1 Å^{-1} in agreement with experimental results (Figure 3A). Furthermore, our simulations are also in agreement with the diffraction data for Q> 1, see Figure S2 in the SI. This further supports our previous observations(17) that the nanostructuring observed in these simulations is consistent with that of the CO_2-loaded solvent.

As observed in Figure 3B, there is a qualitative difference between the diffraction peaks at $Q < 0.7$ Å^{-1} that we attribute to the simulation size effect. However, due to limitations in simulation cell size (8x8x8 nm). Figure S3 in the SI shows how the low Q structure becomes smoother in the larger simulation cells. Understanding the composition and structure of these species could help describe the mechanisms for the proposed glassification within the solvent, though observing any large-scale supramolecular assembly was beyond the size resolution limit of both the ND experiment and the simulations.

### Small Angle Neutron Scattering (SANS)

Lower Q data was needed to assess how nm-scale interactions impact larger scale ordering in solution. As such, SANS measurements on Larmor sought to describe the behavior and properties of these aggregates and nanoclusters as a function of temperature and CO_2 content. Initial measurements carried out from 22–100°C in 20°C increments showed no large aggregates in the measured Q range (details of SANS experiment contained in the SI). CO_2-loaded hydrogenated and neutraldeuterated mixtures (Fig.2 a and d, respectively) showed only a liquid background signal that decayed on average as $Q^{-1.65}$, with a radius of gyration, R_g, of 10 to 11 Å. A scattering exponent of $Q^{-5/3}$ is expected for swollen chains in solution, so the observed dependence could indicate that molecular dimers characterized by dimension R_g may cluster to form chains throughout the liquid. Beyond this, the inability to detect any larger scale clustering was likely due to a combination of having short-lived intermolecular association due to the system's high thermal energy and that the density of such clustering was too low to result in any appreciable difference in scattering length density contrast between clusters and the surrounding homogeneous solvent.

Hypothesizing that at low temperatures the zwitterionic dimers would not have enough kinetic energy to overcome aggregation forces and result in an aggregate structure that is stable in time, we proceeded to carry out measurements from −5°C (the limit of the cooling bath) to 40°C. Our results show the gradual formation of large aggregates with decreasing temperature, while the aggregates reversibly diminished as temperature was increased.

A two-level unified exponential power model(41, 42) was applied to the 1:1 deuterated:hydrogenous CO_2-bound system temperature cycling scattering data to extract details of the reversible aggregate structure (details of the UEP model described in the SI). Figure 4 shows the model parameters as a function of time (and temperature cycling). Parameters from measurements collected in decreasing temperature directions are shaded in blue and measurements collected as a function of increasing temperature are shaded in red.

The first level, $i = 1$, describes scattering from aggregates with size > 50 nm. Because the low-Q signal which increases with low temperature is due to aggregates that are much larger than the

SANS technique's observation window, R_{g1} was fixed at 50 nm as this was the smallest value that would allow the model to fit
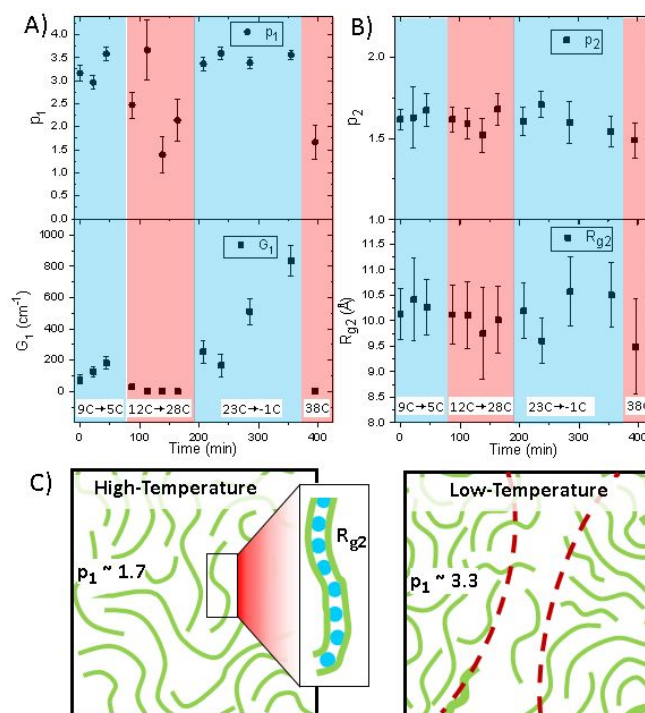
the data satisfactorily. Parameter G_1 (Figure 4A) is related to the concentration of large aggregates as a function of time during the temperature cycling experiment. The G_1 parameter is generally higher for measurements carried out as temperature was decreased and lower when temperature was increased.

Figure 4. (A&B) Two-level unified exponential model fit parameters help describe the fractal nature of the large aggregates (p_1) and relative orientation of the molecules (p_2), the increase in aggregate concentration (G_1), and the static size of molecular clusters over the entire temperature range (R_{g2}). (C) Schematic illustrates changes in the hierarchical structure of the material in transition between low and high temperature.

The R_{g2} parameter (Figure 4B), which likely characterizes the dimensions of dimers, remains relatively constant at approximately 10 Å for all temperatures. Similarly, the p_2 parameter that describes the arrangement of the dimers has an average value of 1.61, which is slightly lower than 5/3, the expected value for a chain-like structure. This suggests that locally the molecules associate asymmetrically with one another, forming a chain-like motif which persists throughout the measured temperatures (Figure 4C). Regions in the liquid that are richer in the chain-like associations are characterized by the G_1 and p_1 parameters (Figure 4A). During the cooling cycles, p_1 varies between 3.0 and 3.6, characteristic of surface scattering from a large structure, while for the heating cycles p_1 varies from 1.4 to 2.5, which is characteristic of mass fractal and polymer-like structures. Thus, during heating the p_1 exponent nearly matches the p_2 exponent and G_1 is at a minimum indicating a homogeneous liquid at large length scales > 50 nm, which is similar to the local structure characterized by the $i = 2$ parameters. During cooling, exponent $p_1 > 3$ and maximum

values of G_1 indicate the presence of > 50 nm regions with a density of 1-IPADM-2-BOL-CO_2 zwitterions that is high enough to form a well-defined albeit rough interface with the surrounding primarily neutral liquid Figure 4C). The rough interface between the neutral and zwitterionic regions matches our previous ToF-SIMs data, which showed that the interface of the >500 nm aggregates (25 °C, 0.25 mol CO_2/mol solvent) was not completely smooth with the non-ionic regions of the fluid.(17) These observations during heating and cooling also suggest aggregation of the small clusters is reversible and temperature dependent, much like a glass transition (further details contained in the Figures S4-S5, SI).

Wide-Angle X-Ray Scattering

Wide angle x-ray scattering (WAXS) of CO_2-free and CO_2-bound (0%, 25%, and 50% by mole CO_2) 1-IPADM-2-BOL were carried out over a Q-range of 0.1 − 2.6 Å-1 along with measurements from 0 to 60 °C for 0% and 50% CO_2-loaded samples (Figure 5). The CO_2-bound liquid shows a structural correlation near Q = 0.36 Å−1 which is absent in the CO_2-free liquid (Figure 5A). This type of intermediate range order corresponds to dimensions which are similar to some low-molecular-weight conventional ionic liquids.(43-45) The degree of disorder indicated by the peak widths of individual correlations is similar to that of ionic liquids. All WAXS data was fitted with a model consisting of 3 Lorentzian peaks for the 0%-CO_2 data and 4 peaks for the 50%-CO_2 data (See Figure S6A in the SI).(46) The largest correlation, d_1, varies from ~17.0 Å to 18.6 Å over the 0 to 60 °C range. From 0–30 °C, d_1 increases slowly at a rate of 0.0011 Å/°C, yet increases 45-fold to a rate of 0.0483 Å/°C from 30–60 °C (Figure 5B). Conversely, correlations d_2, d_3, and d_4 in the 50% CO_2-loaded liquid exhibit higher rates of change from 0–30 °C followed by slower rates from 30–60°C (Figure S6B in the SI). The variation in d_n at low temperature occurs as expected for simple volume expansion of the liquid. As temperature is increased, the d_2–d_4 correlations for the 50% CO_2-loaded samples approach the correlations of the CO_2-free liquid (Figure S6C in the SI), indicating that CO_2 is gradually being removed from the solvent.
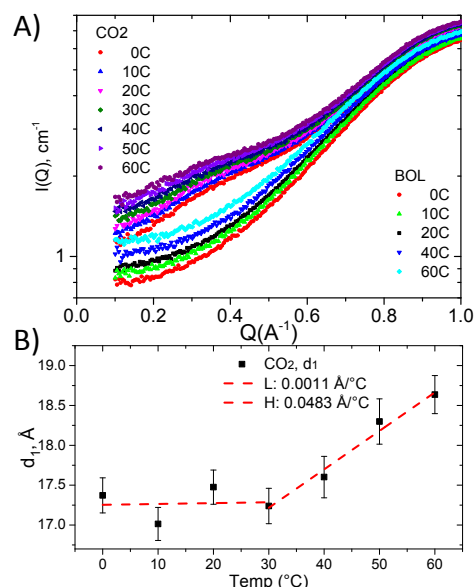

Figure 5. WAXS temperature dependence of molecular length scales. (A) CO_2-loaded sample has a correlation near Q = 0.36 Å^{-1} which is completely absent in the CO_2-free material. (B) The d_1 correlation varies from ~17.0 Å to 18.6 Å from 0 to 60 °C and exhibits a steep 45-fold increase in the rate of change from 30 to 60 °C.

To further validate the structural model represented by the MD, we further analyzed our molecular simulations to determine whether they could identify the specific interactions that drive this phenomenon. The ND data illustrating both the "glassy" and "metastable" fluid states at three temperatures is provided in figure S7, SI, while x-ray diffraction spectra of them at 40 °C are shown in Figure S8, SI. The simulated diffraction curves of the "glassy" state closely align with those of the neutron and x-ray measurements. It is reasonable that the experimental data likely represent the glassy-state of the fluid because the required measuring times do not allow measuring the short-lived metastable states. Otherwise, the simulations reasonably reproduce the trends in the experimental data, showing an increase in Q (smaller range) as temperature increases for both the metastable and glassy states. We then cooled the metastable state and observed the spectra change to match that of the glassy state, indicating the glassification is due to changes in long range order.

Our fitting suggested that the glassy state appears at temperatures near 40 °C or below. To confirm this, we checked the viscosity profile of 1-IPADM-2-BOL in our previously reported continuous flow testing,(27) noting the measured viscosities were comparable to the metastable state (Figure 1). This finding was attributed to being above the transition temperature because the absorber (while jacketed to 40 °C) had fluid exiting the bottom of the column at 45 °C. We then measured an isotherm at 42 ˚C for 1-IPADM-2-BOL using our PVT cell (Figure S9 in the SI). The viscosity data measured in this isotherm correlated with the viscosity of the metastable state,

not the glassy state (both shown in Figure 1). Ultimately, PVT and continuous-flow testing of 1-IPADM-2-BOL at greater than 42 °C confirmed the theoretical prediction that glassification occurs at approximately 40 ˚C.

Transport and rheological properties

Our focus then shifted to identifying changes in the simulated transport and rheological properties of 1-IPADM-2-BOL-CO_2 in both states. The diffusion coefficients of glassy and metastable states were calculated from molecular dynamics simulations and results are provided in Figure 6a. As expected, the diffusion coefficients increase with temperature (noting that the glassy states show lower diffusion coefficients than metastable states at temperatures below 50°C). There is an abrupt leveling of the diffusion coefficient in the metastable state at 40°C until approximately 50°C, where the coefficient in the meta and glassy states begin to converge.

We then aimed to experimentally validate the diffusion coefficients from the molecular dynamics simulations by using pulsed field gradient, diffusion-oriented nuclear magnetic resonance spectroscopy on 1-IPADM-2-BOL, which is a technique sensitive to diffusion over millisecond timescales. Two series of experiments were performed; the first applied ^{13}C PFG NMR at 14.1 T on a sample loaded with ^{13}C-enriched CO_2 to directly resolve zwitterionic species via their ^{13}C resonances ca. 160 ppm. The results (Figure S11) show that the absolute value of the diffusion coefficients obtained with PFG NMR and that of molecular simulations are in fair agreement, where specifically, ^{13}C resonances of 1-IPADM-2-BOL exhibit diffusion coefficients ranging from ca. 0.01–0.03 10^{-5} cm²s⁻¹ at 40 °C and ca. 0.02–0.07 10^{-5} cm²s⁻¹ at 60°C at a loading of 0.2.

The second series of experiments were composed of ^{1}H PFG NMR at 17.6 T on 1-IPADM-2-BOL loaded with natural abundance CO_2 at a loading of 0.2. Analysis was focused on the methyl proton occurring at ca. 1.2 and 1.4 ppm(34) at temperatures ranging from 25 to 100°C, with diffusion coefficients shown in Figure S12, where diffusion coefficients at 40 and 60°C of the methyl resonance were ca. 0.01 and 0.03 10^{-5} cm²s⁻¹, respectively. Given that molecules in glassy regions exhibit efficient relaxation(47, 48) and the PFG NMR measures a convoluted relaxation and population weighted diffusion coefficient, it is likely that the PFG NMR diffusion coefficients acquired are of mestastable states.

We also calculated the viscosity of these systems from the molecular trajectories using Stokes–Einstein equation as shown in Figure 6b. The radius of gyration is used to approximate the radius of a sphere particle in the Stoke-Einstein equation. The simulated viscosity at 40°C of the glassy state (179 cP) and the metastable state (105 cP) is in good qualitative agreement with the experimentally determined values of 410 and 130 cP, respectively. The underestimation may be due to limitations of

the Stokes-Einstein equation, which only accounts for diffusion without explicit collective motions due to intermolecular correlations. However, another reason for the non-quantitative agreement may be that the small simulation cells cannot capture entirely the interaction between large domains. Nevertheless, the simulations suggest clearly different behaviors between the two systems when the temperature is below 40°C and the observed transition from metastable state to glassy state at 40°C increases viscosity in agreement with the experimental data. Similar to the diffusion coefficients, as the temperature further increases above 40°C, the viscosity of the two systems starts to converge and the two states evolve to a similar system. Note that the calculated data using the larger and longer simulation boxes at 40°C and 100°C are still close to the results obtained using the original box of 8³ nm, validating the data obtained in these simulations. These results again reveal the presence of a transition temperature between the metastable and glassy states at 40–50°C and the differences between these two states can be observed only below such temperatures. Having thoroughly characterized this transition, it was still unclear which molecular-level interactions were resulting in these structural changes that introduced a glass-transition in the fluid.
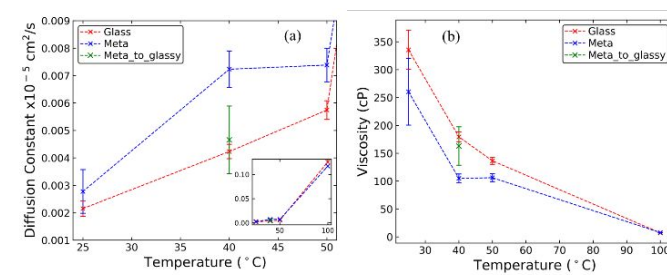

Figure 6. Comparison of (a) diffusion coefficients and (b) viscosity between glassy and metastable states.

Assessing local structure through radial distribution functions

We calculated the radial distribution function, $g(r)$, of zwitterion–zwitterion, zwitterion–neutral, and neutral–neutral pairs, respectively, based on the center of mass of molecules to further understand the structural differences between the glassy and metastable states. We also evaluated the average percentage of zwitterionic neighbors of zwitterions in these structures. An example for $g(r)$ of zwitterion–zwitterion is illustrated in Figure 7. The rest of the data are provided in Figures S13 and S14. At 40 °C, the glassy state suggests a higher populations of zwitterionic neighbors at ~0.45 nm, indicating a strong aggregation of zwitterions as illustrated in Figure S14. The aggregation in both states is reduced at temperatures > 50 °C, and eventually a similar behavior was observed in both systems at 100 °C. The $g(r)$ results suggest that different types of clustering are present in both glassy and metastable states at 25 °C. A stronger aggregation of zwitterions exists in the glassy state as the temperatures increase to 40 °C, and such effect is reduced at the temperatures above 50 °C. The "glassy transition" between 40 °C and 50 °C results in different

distributions of zwitterion/neutral neighbors in the glassy and metastable states, causing distinct behaviors of the two states (as discussed in the previous sections).
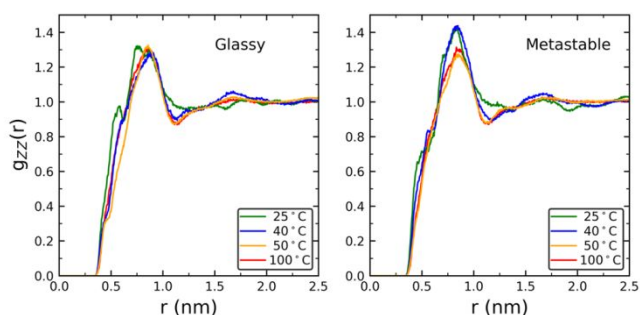

Figure 7. The partial radial distribution function of zwitterion-zwitterion (g_{Z-Z}) in the glassy and metastable states.

Changes in Angle Distributions Between States

To provide additional atomistic-level information regarding how the glass transition impacts the two states, we used two vector parameters in the zwitterion molecules. The first vector points from the positively charged N to the C connected with the negatively charged O. This vector indicates the orientation of the COO⁻ group relative to the guanidium group (H⁺NR). The second indicates the normal direction of the plane defined by the three N atoms (3-N plane) in the zwitterion. With the aid of these two vector parameters, we evaluated the angle (θ) between the COO⁻ group and 3-N plane in each zwitterion, the angles (α) of the COO⁻ groups between zwitterions and their zwitterion neighbors, and the angles (β) of the 3-N planes between zwitterions and their zwitterion neighbors. Figure S15 provides a visual aid for the vector parameters and angles we used here.

The full angle distributions of these angles (θ, α and β) and visual examples of their corresponding zwitterion molecular configurations or zwitterion neighbor pairs with different pairing angles are illustrated in figure S16 and S17, respectively. For angles between the COO⁻ group and the 3-N plane in zwitterions (θ), the glassy state shows slightly lower population of angles between 30° and 55°, but higher population for angles around 55°–75° compared to the metastable state at 25°C. Similarly, at 40°C, the glassy state registers lower polulation of angles angles below 20° and higher population of angles above 20° than the metastable state. This suggests that the COO⁻ groups tend to form larger angles relative to the 3-N planes in the glassy state than those in the metastable state. Both systems show similar angle distributions when the temperatures are above 50°C. For the angle populations of the COO⁻ groups and 3-N planes, respectively, between zwitterions and their neighbors (α and β), the COO⁻ groups of zwitterions in the glassy state tend to form larger populations between 100° and 150° and smaller populations below 100° with the COO⁻ groups of their zwitterion neighbors at temperatures below 40°C. The angles of 3-N planes in these zwitterions also have

larger populations above 50° than the metastable state. Although the results based on the 0.65 nm cutoff reveal the zwitterion pairs more locally, and the results based on 1.1 nm cutoff consider larger spaces around zwitterions, the differences in the angle populations between the glassy and metastable states obey similar trendsregardless of the cutoff. The free energy plots as shown in Figure 8 suggest a single minimum in the glassy state, but multiple local (metastable) minima in the metastable state at 25 °C. Such differences at the molecular scale increase the mobility of zwitterions in the metastable state and eventually lead to the lower viscosity of the metastable state observed in the experiments. As temperature increases above 40 °C, both states converge to a single minimum.

Based on the analysis of the angle distribution, more zwitterions in the glassy state are slightly folded than those in the metastable state. In pairs of zwitterion neighbors, the COO⁻ groups in the glassy state tend to form larger populations of anti-parallel pairs with angles around 130° than in the metastable state, and the 3-N planes in these zwitterions pair less parallelly with angles above 50° compared to the metastable state. Such orientational differences are accompanied by the distinctions of the amounts of external hydrogen bonds. The system-average numbers of external hydrogen bonds in the metastable and glassy states are provided in Figure S18. The data suggest that more external hydrogen bonds are observed between zwitterions in the glassy state compared to the metastable state. These minute changes in the hydrogen bonds lead to the aggregation of zwitterion clusters observed in experiment and are ultimately the root cause for the glassification of 1-IPADM-2-BOL.
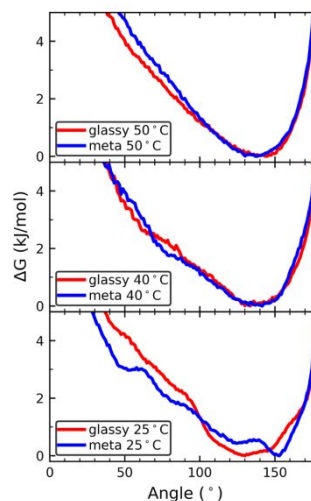

Figure 8. Free energy as a function of angles of the COO⁻ group between zwitterion neighbors within cutoff of 0.65 nm.

It is likely that similar structural changes in orientation of hydrogen bonding in solution are occurring in 1-IPADM-3-BOL and 1-MEIPADM-2-BOL. We postulate that other concentrated or water-lean solvents would exhibit a similar phase transition

if their CO_2-containing ions are not solvated by water or other diluents solution as is the case for aqueous amines.

Discussion: Impacts of glassification on a solvent-based CCS process

The majority of water-lean solvents are configured to run their absorption cycles at approximately 40°C due to the availability of cooling water.[11] Plugging a carbon capture unit could be potentially catastrophic to the capture unit, as gas flow would have to be halted and millions of liters of solvent would have to be heated and drained prior to continued use. To our knowledge there has been no reported glassification of water-lean solvents during testing in routine operation. We attribute the lack of reported glassification to the (−80 kJ/mol)[11] exothermicty of CO_2 capture by thermal-swing solvents. The high enthalpy of CO_2 binding coupled with the low specific heat of organics results in a larger temperature increase of the CO_2-rich solvent by the time it exits the absorber column as compared to aqueous solvents. The self-heating of the solvent during absorption of CO_2 would likely bringing any water-lean solvent above a potential T_g.

Paradoxically, post-combustion solvent researchers and developers (like ourselves) are assessing the benefits of introducing intercooling into the absorber column, as lower temperatures have been shown to improve CO_2 mass transfer (smaller and cheaper equipment)[24] and condense more water from the inlet flue gas, reducing reboiler duty due to reduced water content.[13] Thus, the resulting lower CO_2 absorption temperature presents a trade-off: reduced cost and improved efficiency at the expense of operating solvents precipitously close to T_g during operation. We are currently assessing whether other formulations of water-lean solvents (e.g., amines) exhibit similar phenomena to determine whether glass transitions in water-lean solvents are common and how we could mitigate glass transitions through control of molecular-level structures within these fluids.

Conclusions

In this computational and experimental study, we present the first evidence that post-combustion CO_2 capture solvents, such as 1-IPADM-2-BOL, undergo a first-order phase transition that we liken to a glass transition. Ultimately, we stress the need of molecular-level understanding of solvent behavior to mitigate any potentially limiting behaviors prior to commercial operation. Thus, we encourage those in the field of CCS to assess whether their solvent formulations exhibit a T_g prior to large-scale testing. Identifying a potential glassification provides knowledge that could prevent catastrophic failure of carbon capture infrastructure in large-scale testing or commercial operation. Fortunately, the exothermicity of CO_2 capture in a working solvent-based process could provide enough heating for solvents to operate above a potential T_g, lessening the likelihood of glassification and potential failure in operation. However, this is a phenomenon that can help keep the solvent

in a metastable liquid state, by tailoring the molecular interactions tthat minimize clustering altogether.

Experimental

General Experimental: All the reactions were conducted under an atmosphere of nitrogen unless otherwise indicated. Solvents were transferred via gas-tight syringe, cannula, or dropping funnel. The d_6-propyleneoxide, 1,3-dimethylimidazolidinone, triethylamine, ammonium hydroxide, and dichloromethane were purchased from commercial sources and used without purification. Carbon-13 nuclear magnetic resonance (^{13}C NMR) spectra were recorded with 500 MHz (125.7 MHz) spectrometer. Chemical shifts are reported in delta (δ) units, parts per million (ppm) relative to the center of the triplet at 77.00 ppm for deuterochloroform. ^{13}C NMR spectra were routinely run with broadband. Mass spectra (MS) ESI accurate masses are reported for the molecular ion (M+1) or a suitable fragment ion.

Synthesis of 1-IPADM-2-BOL: 1-IPADM-2-BOL was synthesized by previously reported methods in *RSC Adv.,* (2012), 3, (2), 566-572, while 1-IPADM-3-BOL and 1-MEIPADM-2-BOL were synthesized as described previously.(18)

Synthesis of 1-aminopropan-1,1,2,3,3,3-d_6-2-ol:(49) To a three-neck round bottom flask containing ammonium hydroxide solution, d_6-propyleneoxide was added and reaction was stirred for 2 h at room temperature. The progress of the reaction was monitored by thin-layer chromatography and crude NMR. Excess ammonium hydroxide was removed under reduced pressure followed by distillation to get pure compound -aminopropan-1,1,2,3,3,3-d_6-2-ol (41.4 % yield, 7.85 g, 0.0968 mol). ^{13}C NMR (CDCl$_3$, 125.7 MHz): 19.4 (sep), 48.1 (qui.), 67.2 (t) ppm.

Synthesis of 1-((1,3-dimethylimidazolidin-2-ylidene)amino)propan-1,1,2,3,3,3-d_6-2-ol:(34) To a three-neck round bottom flask fitted with inert nitrogen, containing ice-cooled solution of 1-aminopropan-1,1,2,3,3,3-d_6-2-ol (7.42g, 0.0915 mol) in anhydrous dichloromethane (50 ml), trimethylamine (26 mL, 0.1887 mol) was added followed by the dropwise addition of a solution of 2- Chloro-1,3-dimethylimidazolinium chloride (17 g, 0.107 mol) in dichloromethane (20 ml). The reaction mixture was warmed to room temperature, stirred for 24 h, and refluxed for a further 48 h. The reaction was cooled to room temperature and extracted thrice with 30% aqueous KOH. The combined organic extracts were dried over anhydrous MgSO$_4$, filtered, and the solvent was removed under reduced pressure to afford yellowish liquid which was further purified via distillation under reduced pressure to yield pure compound 1-((1,3-dimethylimidazolidin-2-ylidene)amino)propan-1,1,2,3,3,3-d_6-2-ol (66.5% yield, 10.77 g, 0.061 mol). ^{13}C NMR (CDCl$_3$, 125.7 MHz): 18.8 (sep), 35.8 (d), 36.0 (d), 49.1 (d), 49.6 (d), 53.5 (qui.), 66.6 (t), 157.9 ppm. MS calculated [M+H$^+$] for $C_8H_{12}D_6N_3O^+$ is 178.2 and found 178.2.

SANS: Measurements were carried out at the Larmor beamline on Target Station 2 of the ISIS pulsed neutron source at the Rutherford Appleton Laboratory, Didcot, UK, using a sample changer and 1 mm and 2 mm path length quartz cuvette cells, for hydrogenous and deuterated samples, respectively. In SANS, intensity as a function of the scattering vector Q is collected with $Q = (4\pi/\lambda)\sin(\theta)$. Here, 2θ is the scattering angle, and λ is the neutron wavelength range of 0.9–12.5 Å used simultaneously by time of flight. The Q range for this experiment was 0.004–0.8 Å^{-1}. The instrument was in the 4 m sample-detector configuration, with A1 = 20 mm^2, S1 = 14 mm^2, and a sample aperture of 6 mm (horizontal) by 8 mm (vertical). Typical data collection times on Larmor were 15 min. Measurements on Larmor were carried out in event mode and data sets were sliced into 2-minute intervals to observe any time dependence in the SANS signal. Data reduction was performed using Mantid(50) and scattering simulations fitted using SasView v4.2.2.0.(45, 46)

Neutron Diffraction: Diffraction data were collected using NIMROD, located in Target Station 2 at the ISIS Neutron and Muon Source, Rutherford Appleton Laboratory, Harwell Campus, UK under allocations RB1610024 and RB1610023. NIMROD provides and a wide Q range for accessing correlations between <0.1 nm and approximately 30 nm. Data were collected over the full Q-range of 0.1 to 50 Å^{-1}. Samples were loaded into null-scattering, vacuum sealed TiZr alloy 1 mm sample pathlength flat plate cells. A vanadium standard, the empty instrument, and empty sample cells were measured in addition to the samples for data normalization and instrument calibration. The samples were placed on a copper bracket which was temperature controlled using a circulating fluid bath. GudrunN, an analysis suite based on the ATLAS software package, was used to correct raw neutron total scattering data for multiple-scattering and beam attenuation and normalize to an absolute scale.(51) Due to the high hydrogen content of the samples, particular attention was paid to correcting for inelasticity effects, which were removed using an iterative approached developed by Soper.(52)

SAXS: SAXS measurements were carried out using a Xeuss 2.0 HR SAXS/WAXS system (Xenocs, Sassenage, France) with a Cu source tuned to λ = 0.1542 nm. The neat and CO$_2$-loaded 1-IPADM-2-BOL materials were each loaded into 1 mm path length, thin-wall, boron-rich glass capillaries, which were then sealed using hot glue. Two sample-to-detector distances (sd) of 156 mm and 1209 mm, to span a Q-range of 0.009–2.68 Å^{-1}. In SAXS, X-rays scattered as a function of the scattering angle 2θ, with respect to the transmitted direct beam, are collected on an area detector. The two-dimensional data is azimuthally averaged and plotted as I(Q). Here, Q is given by $Q = 4\pi\sin\theta/\lambda$, where θ is half the scattering angle, and Q is related to the size of the scattering object d as $Q \sim 1/d$. Data were collected for 1800 s at sd 1209 mm and 600 s at sd 156 mm to obtain the counting statistics shown in the plots. Scattering the empty glass capillary was used as the background measurement and subtracted from the presented data. The SAXS intensity I(Q) was scaled to units of differential scattering cross section per unit volume (cm^{-1}) using a glassy carbon intensity calibration standard.(53)

CO$_2$ loading and viscosity measurements: A custom test cell developed in-house was used for vapor liquid equilibrium

measurements concurrently with viscosity. In a typical experiment, the liquid sample in its CO_2-free form is loaded into the temperature-controlled test cell and recirculated by a mechanical gear pump under vacuum to remove any dissolved gases. Once the pressure has stabilized, metered amounts of CO_2 gas are injected into the cell vapor phase through an automated valve manifold from a calibrated 150 mL volume and allowed to be absorbed by the liquid sample until a new equilibrium state is reached. The measurements are repeated until the sample is fully saturated with CO_2. The viscosity of liquid is measured using an in-line viscometer (Cambridge ViscoPro 2000) installed on the liquid circulation loop. The viscometer had a model 372 sensor with a 50-1,000 cP piston head installed during operation. Accuracy of this instrument is within +/- 1% full scale. The cell pressure is measured within an accuracy of 0.2% using Nor-Cal CDG-100 series pressure transducers. The CO_2 loading in the liquid phase at each equilibrium point is determined from the mass balance–based gas-phase pressure change and known cell volume.

Diffusion Measurements: The ^{13}C and ^{1}H NMR samples were prepared by saturating a solution of 1-IPADM-2-BOL with CO_2 and then adding a CO_2 free aliquot to produce a solution with a loading of approximately 0.2 moles CO_2 per mole of 1-IPADM-2-BOL. Proton decoupled ^{13}C pulsed field gradient NMR was performed with a 5 mm liquid NMR probe (Doty Scientific Instrument, USA) at a field strength of 14.1 T on an Agilent spectrometer, which corresponds with a ^{13}C Larmor frequency of ca. 151 MHz. A vendor-supplied, bipolar gradient pulse pair stimulated echo (Dbppste) pulse sequence was used. For both acquisitions at 40 and 60°C, the spatially dependent gradient pulse duration was 2.0 ms and the delay between spatially dependent gradient pulses was 50 ms. The delay between scans was 5 s, the acquisition time was 50 ms, and 512 transients were collected. The ^{13}C PFG NMR spectra were analyzed in vNMRJ (v. 4.2) where 50 Hz of line broadening was applied.

^{1}H pulsed field gradient NMR was performed with a 5 mm broadband observe (BBO) NMR probe at a field strength of 17.6 T on an Agilent spectrometer, which corresponds with a ^{1}H Larmor frequency of ca. 750 MHz. A vendor-supplied, DOSY gradient compensated stimulate echo with spin lock with convection compensation (DgcsteSL_cc) pulse sequence was used. Temperature was calibrated using the ^{1}H chemical shifts of ethylene glycol[54] and diffusion coefficients are referenced to water (H_2O) at 25°C.[55] For acquisitions at 20, 25, 40, 50, 60, 70, 80, 90, and 100°C, the spatially dependent gradient pulse duration was 11, 11, 7.8, 5.5, 3.8, 2.9, 2.2, 1.9, and 1.7 ms, respectively with a delay between spatially dependent gradient pulses of 200 ms. Additional experiments with a diffusion delay of 250 ms at temperatures of 25, 40, 50, 60, 80, 90, and 100°C used a gradient pulse duration of 9.8, 7.1, 4.9, 3.4, 2.0, 1.7 and 1.5 ms. For experiments with either diffusion delay, the acquisition time was 367 ms, the delay between scans was 1.4 s, 32 increments in gradient strength were used, and 8 transients were collected for each increment. At each temperature, the pulse length corresponding to a $\pi/2$ pulse was calibrated. ^{1}H PFG NMR spectra were analyzed in vNMRJ where 2 Hz of line broadening was applied. For both ^{13}C and ^{1}H datasets, the spline modelling (SPLMOD) routine was applied to

determined diffusion coefficients from integrated resonances. Additional experimental details and results for supporting ^{1}H – ^{13}C gradient heteronuclear single quantum correlation (gHSQC) NMR acquired at a field strength of 9.4 T at 40°C on an unreacted 1-IPADM-2BOL sample are included in Figure S10.

Classical MD and viscosity calculations: Classical MD simulations of CO_2BOL solvents at various CO_2 loadings were done at 40°C to calculate viscosities, self-diffusion coefficients, and dielectric constants. CO_2-loaded molecules were modeled by either all zwitterionic, half zwitterionic half acid, or all acid species that allowed us to gauge how non-ionic acid-state CO_2-bound CO_2BOLs change solvent viscosity.

The GROMACS(56) package version 4.6.6 was used for all classical MD simulations. Optimized geometries and charges obtained from electronic structure calculations were used with the OPLS-AA(57) force field. Certain dihedral angle parameters were obtained from electronic structure calculations (see SI). Mixtures of CO_2-bound and unbound CO_2BOLs were constructed at varying carbon loadings (mol%: 0, 10, 15, 20, 25, 30), with a total of 1,728 molecules. Energy minimizations and high-temperature runs for proper mixing were done, followed by NPT ensemble equilibrations at 1 bar and 40°C until the volume and total energy display steady-state behavior, typically occurring between 5 and 10 ns of simulation.

Viscosities were calculated using the Stokes-Einstein relation. The radius of gyration of the solvent molecule is used to estimate the radius of particles in the equation. The recently proposed approach(61) to calculate viscosity in two-component ionic liquids, based on ion pair lifetimes, is not compatible with single-molecule solvent systems. Self-diffusion coefficients and dielectric constants were also calculated starting from equilibrated frames with programs in GROMACS suite.

Conflicts of interest

There are no conflicts to declare.

Acknowledgements

and the Environmental Molecular Science Laboratory (EMSL, grid.436923) at PNNL.

Notes and references

1. Climate Change 2014 Mitigation of Climate Change, Working Group III Contribution to the Fifth Assessment Report of the Intergovernmental Panel on Climate Change, https://www.ipcc.ch/site/assets/uploads/2018/02/ipcc_wg3_ar5 _full.pdf

2. P. Friedlingstein *et al.*, Global Carbon Budget 2019. *Earth Syst. Sci. Data* **11**, 1783-1838 (2019).

3. M. Bui *et al.*, Carbon capture and storage (CCS): the way forward. *Energy & Environmental Science* **11**, 1062-1176 (2018).

4. A. L. Kohl, R. B. Nielsen, "Preface" in Gas Purification (Fifth Edition)*, A. L. Kohl, R. B. Nielsen, Eds. (Gulf Professional Publishing, Houston, 1997), https://doi.org/10.1016/B978-088415220-0/50000-8, pp. vii-viii.

5. Carbon Capture & Sequestration Technologies at MIT, Petra Nova W.A. Parish Fact Sheet: Carbon Dioxide Capture and Storage Project, https://sequestration.mit.edu/tools/projects/ wa_parish.html, 2016, accessed on January 20, 2017.

6. NRG. News Release: NRG Energy, JX Nippon Complete World's Largest Post-Combustion Carbon Capture Facility On-Budget and On-Schedule, http://investors.nrg.com/phoe nix.zhtml?c=121544 p=irol-newsArticle ID=2236424, 2017, accessed on February 6, 2017.

7. U.S. Department of Energy, National Energy Technology Laboratory (NETL), Recovery Act: Petra Nova Parish Holdings: W.A. Parish Post-Combustion CO2 Capture and Sequestration Project, https://www.netl.doe.gov/research/coal/project-information/fe0003311, 2016, accessed on February 6, 2017.

8. U.S. Office of Fossil Energy, Petra Nova – W.A. Parish Project. https://energy.gov/fe/petra-nova-wa-parish-project, 2017, Accessed on January 17, 2017.

9. Carbon Capture & Sequestration Technologies at MIT, Kemper County IGCC Fact Sheet: Carbon Dioxide Capture and Storage Project, http://sequestration.mit.edu/tools/projects/kemper.html, 2016, accessed on February 16, 2017.

10. H. Herzog, Lessons Learned from CCS Demonstration and Large Pilot Projects: An MIT Initiative Working Paper, MIT Energy Initiative, Massachusetts Institute of Technology, 2016.

11. D. J. Heldebrant *et al.*, Water-Lean Solvents for Post-Combustion CO_2 Capture: Fundamentals, Uncertainties, Opportunities, and Outlook. *Chem. Rev.* **117**, 9594-9624 (2017).

12. M. Lail, J. Tanthana, L. Coleman, Non-Aqueous Solvent (NAS) CO_2 Capture Process. *Energy Procedia* **63**, 580-594 (2014).

13. P. M. Mathias *et al.*, Improving the regeneration of CO_2-binding organic liquids with a polarity change. *Energy Environ. Sci.* **6**, 2233-2242 (2013).

14. Yuan, Ye and Rochelle, Gary, Water-Lean Solvents for CO_2 Capture Will Not Use Less Energy than Aqueous Amines. 14th Greenhouse Gas Control Technologies Conference Melbourne 21-26 October 2018 (GHGT-14) . Available at SSRN: https://ssrn.com/abstract=3366219

15. M. J. O'Brien, R. L. Farnum, R. J. Perry, CO_2 Capture Using 2,2-Dialkylpropane-1,3-diamines. *Energy Fuels* **27**, 467-477 (2013).

16. D. Malhotra *et al.*, Phase-Change Aminopyridines as Carbon Dioxide Capture Solvents. *Ind. Eng. Chem. Res.* **56**, 7534-7540 (2017).

17. X.-Y. Yu *et al.*, Mesoscopic Structure Facilitates Rapid CO2 Transport and Reactivity in CO_2 Capture Solvents. *J. Phys. Chem. Lett.* **9**, 5765-5771 (2018).

18. D. Malhotra *et al.*, Reinventing Design Principles for Developing Low-Viscosity Carbon Dioxide-Binding Organic Liquids for Flue Gas Clean Up. *ChemSusChem* **10**, 636-642 (2017).

19. J. Yao *et al.*, Two coexisting liquid phases in switchable ionic liquids. *Phys.Chem.Chem.Phys.* **19**, 22627-22632 (2017).

20. C. Wang, H. Luo, X. Luo, H. Li, S. Dai, Equimolar CO_2 capture by imidazolium-based ionic liquids and superbase systems. *Green Chemistry* **12**, 2019-2023 (2010).

21. D. J. Heldebrant *et al.*, Evaluating Transformational Solvent Systems for Post-combustion CO_2 Separations. *Energy Procedia* **63**, 8144-8152 (2014).

22. D. C. Cantu *et al.*, Dynamic Acid/Base Equilibrium in Single Component Switchable Ionic Liquids and Consequences on Viscosity. *J. Phys. Chem. Lett.* **7**, 1646-1652 (2016).

23. D. Malhotra *et al.*, Directed Hydrogen Bond Placement: Low Viscosity Amine Solvents for CO_2 Capture. *ACS Sustainable Chem. Eng.* **7**, 7535-7542 (2019).

24. P. M. Mathias *et al.*, Measuring the Absorption Rate of CO_2 in Nonaqueous CO_2-Binding Organic Liquid Solvents with a Wetted-Wall Apparatus. *ChemSusChem* **8**, 3617-3625 (2015).

25. G. A. Whyatt *et al.*, Measuring CO_2 and N_2O Mass Transfer into GAP-1 CO_2–Capture Solvents at Varied Water Loadings. *Ind. Eng. Chem. Res.* **56**, 4830-4836 (2017).

26. D. C. Cantu *et al.*, Structure–property reduced order model for viscosity prediction in single-component CO_2-binding organic liquids. *Green Chem.* **18**, 6004-6011 (2016).

27. F. Zheng *et al.*, Bench-Scale Testing and Process Performance Projections of CO_2 Capture by CO_2–Binding Organic Liquids (CO_2BOLs) with and without Polarity-Swing-Assisted Regeneration. *Energy Fuels* **30**, 1192-1203 (2016).

28. J. R. Switzer *et al.*, Design, Synthesis, and Evaluation of Nonaqueous Silylamines for Efficient CO_2 Capture. *ChemSusChem* **7**, 299-307 (2014).

29. V. Blasucci *et al.*, One-component, switchable ionic liquids derived from siloxylated amines. *Chem. Commun.* 10.1039/B816267K, 116-118 (2009).

30. V. M. Blasucci, R. Hart, P. Pollet, C. L. Liotta, C. A. Eckert, Reversible ionic liquids designed for facile separations. *Fluid Phase Equilib.* **294**, 1-6 (2010).

31. A. L. Rohan *et al.*, The Synthesis and the Chemical and Physical Properties of Non-Aqueous Silylamine Solvents for Carbon Dioxide Capture. *ChemSusChem* **5**, 2181-2187 (2012).

32. J. R. Switzer *et al.*, Reversible Ionic Liquid Stabilized Carbamic Acids: A Pathway Toward Enhanced CO_2 Capture. *Ind. Eng. Chem. Res.* **52**, 13159-13163 (2013).

33. V. Blasucci *et al.*, Single component, reversible ionic liquids for energy applications. *Fuel* **89**, 1315-1319 (2010).

34. P. K. Koech *et al.*, Low viscosity alkanolguanidine and alkanolamidine liquids for CO_2 capture. *RSC Adv.* **3**, 566-572 (2013).

35. K. Nishikawa, H. Hayashi, T. Iijima, Temperature dependence of the concentration fluctuation, the Kirkwood-Buff parameters, and the correlation length of tert-butyl alcohol and water mixtures studied by small-angle x-ray scattering. *J. Phys. Chem.* **93**, 6559-6565 (1989).

36. M. Misawa *et al.*, A visualized analysis of small-angle neutron scattering intensity: concentration fluctuation in alcohol-water mixtures. *J. Appl. Cryst.* **40**, s93-s96 (2007).

37. G. D'Arrigo, J. Teixeira, Small-angle neutron scattering study of D$_2$O–alcohol solutions. *J. Chem. Soc., Faraday Trans.* **86**, 1503-1509 (1990).

38. D. T. Bowron *et al.*, NIMROD: The Near and InterMediate Range Order Diffractometer of the ISIS second target station. *Rev. Sci. Instrum.* **81**, 033905 (2010).

39. W. L. Jorgensen, J. Chandrasekhar, J. D. Madura, R. W. Impey, M. L. Klein, Comparison of simple potential functions for simulating liquid water. *J. Chem. Phys.* **79**, 926-935 (1983).

40. B. L. Bhargava, R. Devane, M. L. Klein, S. Balasubramanian, Nanoscale organization in room temperature ionic liquids: a coarse grained molecular dynamics simulation study. *Soft Matter* **3**, 1395-1400 (2007).

41. G. Beaucage, Small-Angle Scattering from Polymeric Mass Fractals of Arbitrary Mass-Fractal Dimension. *J. Appl. Cryst.* **29**, 134-146 (1996).

42. G. Beaucage, Approximations Leading to a Unified Exponential/Power-Law Approach to Small-Angle Scattering. *J. Appl. Cryst.* **28**, 717-728 (1995).

43. R. Hayes, G. G. Warr, R. Atkin, Structure and Nanostructure in Ionic Liquids. *Chem. Rev.* **115**, 6357-6426 (2015).

44. S. Li *et al.*, Alkyl Chain Length and Temperature Effects on Structural Properties of Pyrrolidinium-Based Ionic Liquids: A Combined Atomistic Simulation and Small-Angle X-ray Scattering Study. *J. Phys. Chem. Lett.* **3**, 125-130 (2012).

45. S. Li *et al.*, Toward understanding the structural heterogeneity and ion pair stability in dicationic ionic liquids. *Soft Matter* **10**, 9193-9200 (2014).

46. Doucet, Mathieu; Cho, Jae Hie; Alina, Gervaise; Bakker, Jurrian; Bouwman, Wim; Butler, Paul; Campbell, Kieran; Gonzales, Miguel; Heenan, Richard; Jackson, Andrew; Juhas, Pavol; King, Stephen; Kienzle, Paul; Krzywon, Jeff; Markvardsen, Anders; Nielsen, Torben; O'Driscoll, Lewis; Potrzebowski, Wojciech; Ferraz Leal, Ricardo; Richter, Tobias; Rozycko, Piotr; Snow, Tim; Washington, Adam; SasView version 4.2.2, DOI={10.5281/zenodo.2652478}, Figshare, 2019.

47. W. S. Price, F. Tsuchiya, Y. Arata, Time Dependence of Aggregation in Crystallizing Lysozyme Solutions Probed Using NMR Self-Diffusion Measurements. *Biophys. J.* **80**, 1585-1590 (2001).

48. W. S. Price, Pulsed-field gradient nuclear magnetic resonance as a tool for studying translational diffusion: Part II. Experimental aspects. *Concepts Magn. Reson* **10**, 197-237 (1998).

49. Z. Guangyou, L. Yuquing, W. Zhaohui, H. Nohira, T. Hirose, Resolution of β-aminoalcohols and 1,2-diamines using fractional crystallization of diastereomeric salts of dehydroabietic acid. *Tetrahedron: Asymmetry* **14**, 3297-3300 (2003).

50. O. Arnold *et al.*, Mantid—Data analysis and visualization package for neutron scattering and μ SR experiments. *Nuclear Instruments and Methods in Physics Research Section A: Accelerators, Spectrometers, Detectors and Associated Equipment* **764**, 156-166 (2014).

51. A. K. Soper, GudrunN and GudrunX: Programs for Correcting Raw Neutron and X-ray Diffraction Data to Differential Scattering Cross Section, Rutherford Appleton Laboratory Technical, RAL-TR-201, 2011.

52. A. K. Soper, The Radial Distribution Functions of Water as Derived from Radiation Total Scattering Experiments: Is There Anything We Can Say for Sure? *ISRN Physical Chemistry* **2013**, 279463 (2013).

53. F. Zhang *et al.*, Glassy Carbon as an Absolute Intensity Calibration Standard for Small-Angle Scattering. *Metall. Mater. Trans. A* **41**, 1151-1158 (2010).

54. D. S. Raiford, C. L. Fisk, E. D. Becker, Calibration of methanol and ethylene glycol nuclear magnetic resonance thermometers. *Anal. Chem.* **51**, 2050-2051 (1979).

55. M. Holz, H. Weingartner, Calibration in accurate spin-echo self-diffusion measurements using 1H and less-common nuclei. *J. Magn. Reson.* **92**, 115-125 (1991).

56. D. Van der Spoel *et al.*, GROMACS: Fast, flexible, and free. *J. Comput. Chem.* **26**, 1701-1718 (2005).

57. W. L. Jorgensen, D. S. Maxwell, J. TiradoRives, Development and testing of the OPLS all-atom force field on conformational energetics and properties of organic liquids. *J. Am. Chem. Soc.* **118**, 11225-11236 (1996).

58. R. Zwanzig, TIME-CORRELATION FUNCTIONS AND TRANSPORT COEFFICIENTS IN STATISTICAL MECHANICS. *Annu. Rev. Phys. Chem.* **16**, 67-102 (1965).

59. B. Hess, Determining the shear viscosity of model liquids from molecular dynamics simulations. *J. Chem. Phys.* **116**, 209-217 (2002).

60. T. I. Morrow, E. J. Maginn, Molecular dynamics study of the ionic liquid 1-n-butyl-3-methylimidazolium hexafluorophosphate. *J. Phys. Chem. B* **106**, 12807-12813 (2002).

61. Y. Zhang, E. J. Maginn, Direct Correlation between Ionic Liquid Transport Properties and Ion Pair Lifetimes: A Molecular Dynamics Study. *J. Phys. Chem. Lett.* **6**, 700-705 (2015).